Complete Characterization of Quantum-Optical Processes

Mirko Lobino, Dmitry Korystov, Connor Kupchak, Eden Figueroa, Barry C. Sanders, A. I. Lvovsky*

The technologies of quantum information and quantum control are rapidly improving, but full exploitation of their capabilities requires complete characterization and assessment of processes that occur within quantum devices. We present a method for characterizing, with arbitrarily high accuracy, any quantum optical process. Our protocol recovers complete knowledge of the process by studying, via homodyne tomography, its effect on a set of coherent states, that is, classical fields produced by common laser sources. We demonstrate the capability of our protocol by evaluating and experimentally verifying the effect of a test process on squeezed vacuum.

Construction of a complex machine requires precise characterization of each component's properties. In electronics, this information is obtained from network analyzers, which measure circuit response to simple oscillatory inputs and reveal the device transfer function. Optical quantum technologies, which can be used to build quantum computers (1), precise metrological systems (2), and unconditionally secure communication (3), have similar characterization requirements. In this context, we are interested in the process associated with a quantum circuit component, that is, in being able to predict the transformation that an arbitrary quantum state will undergo when subjected to the action of the component.

A quantum process $\mathcal{E}$ can be represented by a completely positive, trace-preserving linear map (superoperator) on the linear space $\mathbb{L}(\mathbb{H})$ of all density matrices over Hilbert space $\mathbb{H}$. It can be expressed as a rank-4 tensor that relates the matrix elements of the output $\mathcal{E}(\hat{\rho})$ and input $\hat{\rho}$ states in some basis:

$$[\mathcal{E}(\hat{\rho})]_{lk} = \sum_{nm} \mathcal{E}_{lk}^{nm} \rho_{nm} \qquad (1)$$

where summation is from 1 to dim $\mathbb{H}$.

Characterization of a process (known as quantum process tomography or QPT) means finding all components of the superoperator tensor. It can be implemented by determining the output state for each of the $(\dim \mathbb{H})^2$ elements of a spanning set of $\mathbb{L}(\mathbb{H})$. Such a direct approach to QPT (4) was experimentally realized on one-qubit teleportation (5), the Hamiltonian evolution of vibrational states of atoms in an optical lattice (6), and is fine on a two-qubit controlled-NOT gate (7, 8) and Bell-state filter (9). As an alternative, ancilla-assisted QPT exploits an isomorphism between processes and states (10) and has been used to characterize a controlled-NOT gate (11) and a general single qubit gate (12, 13);

Institute for Quantum Information Science, University of Calgary, Calgary, Alberta T2N 1N4, Canada.

*To whom correspondence should be addressed. E-mail: lvov@ucalgary.ca

see (14) for a comparative review of ancilla-assisted QPT.

Existing QPT suffers from serious shortcomings, including either the requirement of an unwieldy set of input states for direct QPT or a high-dimensional entangled input state for ancilla-assisted QPT; these shortcomings deleteriously affect scalability and restrict accessible systems to very low dimension. In optics, QPT has been applied to processes on one and two dual-rail qubits, with postselection based on photon coincidences projecting the input and output states onto these qubit subspaces. This approach cannot provide complete information about a state or a process because optical losses, imperfect sources, detector dark counts, and other imperfections lead to departure from the qubit subspaces. Postselected tomography can only estimate the fraction of such phenomena by comparing the coincidence rate and the photon production rate (9).

We introduce a scheme that enables complete characterization of a general quantum-optical process. We used optical homodyne tomography followed by maximum likelihood reconstruction to obtain full information on the process across all photon number sectors and also the coherence between sectors. The state reconstruction algorithm provides an efficient method for compensating losses in homodyne detection (15). As inputs, we used only coherent states that are readily available from a laser source, so our method can be easily scaled up.

We experimentally tested our approach by characterizing a quantum process that consists of a simultaneous absorption and phase shift. The reconstructed superoperator allows us to predict, with a fidelity of over 99%, the effect of the process on a squeezed vacuum.

Our method has its basis in the fact that any density matrix can be represented as a sum of coherent states' density matrices (16, 17). Although such a representation (the Glauber-Sudarshan P function) may be highly singular, it can be arbitrarily closely approximated with a regular P function. By measuring the process output for many coherent states and exploiting the linearity, we can predict the process output for any arbitrary state.

The Glauber-Sudarshan decomposition of a quantum state $\hat{\rho}$ is given by

$$\hat{\rho} = 2\int P_\rho(\alpha)|\alpha\rangle\langle\alpha|d^2\alpha \qquad (2)$$

where $P_\rho(\alpha)$ is the state's P function, α is the coherent state with mean position, and momentum observables $(x, p) = (\sqrt{2}\,\mathrm{Re}\,\alpha, \sqrt{2}\,\mathrm{Im}\,\alpha)$. We used the convention $[\hat{x}, \hat{p}] = i$, and integration is performed over the entire phase space. Therefore, if we know the effect $|\alpha\rangle\langle\alpha| \mapsto \hat{\varrho}(\alpha) = \mathcal{E}(|\alpha\rangle\langle\alpha|)$ of the process on all coherent states, we can predict its effect on state $\hat{\rho}$:

$$\mathcal{E}(\hat{\rho}) = 2\int P_\rho(\alpha)\hat{\varrho}(\alpha)d^2\alpha \qquad (3)$$

An obstacle to direct application of this approach is posed by singular behavior of the function $P_\rho(\alpha)$. Indeed, the P function exists only as a generalized function, more singular than the Dirac delta function, when the corresponding quantum state has nonclassical features (18).

This can be overcome by applying a theorem proven by Klauder (19): For any bounded operator $\hat{\rho}$, there exists an operator $\hat{\rho}_L$ with continuous and rapidly decreasing P function arbitrarily close to $\hat{\rho}$ in the trace-class norm. The Klauder approximation is obtained as follows: We assume that the Wigner function of $\hat{\rho}$ belongs to the Schwartz class $\mathcal{S}^2$, that is, is infinitely smooth and rapidly decreasing (which is the case for all physically plausible density matrices). The Fourier transform of the operator's Glauber-Sudarshan function $P_\rho(\alpha)$ can be expressed as (18)

$$\tilde{P}_\rho(k_x, k_p) = \tilde{W}_\rho(k_x, k_p)\,\exp\left(\frac{k_x^2 + k_p^2}{4}\right) \qquad (4)$$

where $\tilde{W}_\rho(k_x, k_p)$ is the Fourier transform of the operator's Wigner function. The function defined by Eq. 4 always exists and is infinitely smooth (albeit not necessarily square integrable). We multiply $\tilde{P}_\rho(k_x, k_p)$ by a regularizing function

$$G_L(k_x, k_p) =$$
$$e^{-\left[f(k_x - L) + f(-k_x - L) + f(k_p - L) + f(-k_p - L)\right]}$$
$$\qquad (5)$$

with $f(y) = y^4\exp(-1/y^2)$ for $y > 0$, $f(y) = 0$ for $y \leq 0$. This regularizing function is equal to 1 in a square domain of side $2L$ and rapidly drops to zero outside. The product $\tilde{P}_{L,\rho}(k_x, k_p) = \tilde{P}_\rho(k_x, k_p)G(k_x, k_p)$ now belongs to the Schwartz class. Applying the inverse Fourier transform, we obtain the new Glauber-Sudarshan function $P_{L,\rho}(\alpha)$, which defines the Klauder approximation $\hat{\rho}_L$. By choosing L sufficiently high (20), the operator $\hat{\rho}_L$ can be made to approximate $\hat{\rho}$ arbitrarily well (fig. S1A).

As an example, we applied the Klauder approximation to squeezed vacuum, a nonclassical state characterized by a highly singular P function whose Fourier transform grows exponentially with increasing k_x and/or k_p. We tested our protocol with a state that has a noise reduction in

Fig. 1. Regularized Glauber-Sudarshan decomposition of the squeezed state. (**A**) Absolute value of the regularized Fourier transform of the squeezed vacuum P function. (**B**) Approximated P function calculated from the inverse Fourier transform of $\tilde{P}_{L,\rho}(k_x, k_p)$. (**C** and **D**) Wigner representations of, respectively, the measured and the approximated squeezed vacuum states.
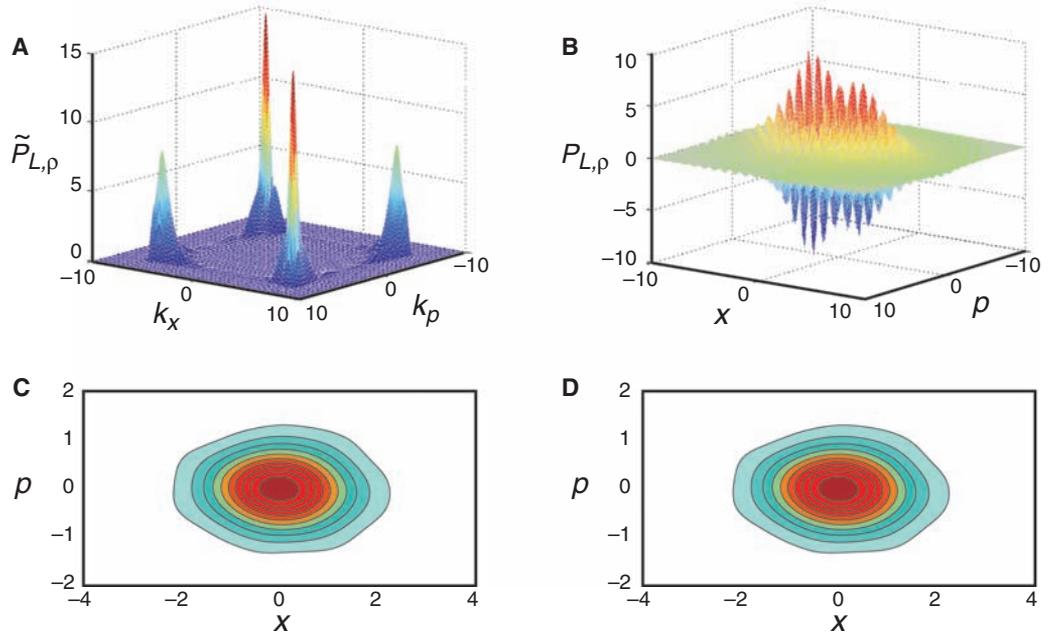
the squeezed quadrature of -1.58 dB and excess noise in the orthogonal quadrature of 2.91 dB. The function $\tilde{P}(k_x, k_p)$ was calculated from the state's density matrix according to Eq. 4 and subsequently regularized as described above using $L = 5.2$. Figure 1A shows $\tilde{P}_L(k_x, k_p)$ calculated from our experimental data, and Fig. 1B displays its inverse Fourier transform $P_L(\alpha)$. In Fig. 1, C and D, we compare the Wigner functions of the original state and the one obtained from the regularized P function. The two states exhibit a quantum fidelity of more than 0.9999.

Although the above method permits finding the process output for an arbitrary input state, it requires one to first determine the input state's P function. This step can be avoided by calculating the process superoperator in the Fock basis, so the output can be found from the input density matrix according to Eq. 1. To this end, we express the Glauber-Sudarshan function as

$$P_\rho(\alpha) = \sum_{mn} \rho_{nm} P_{nm}(\alpha) \qquad (6)$$

where $P_{nm}(\alpha)$ is the P function of the operator $|n\rangle \langle m|$. We now replace these functions by their regularized versions $P_{L,nm}(\alpha)$ and rewrite Eq. 3 as

$$\mathcal{E}(\hat{\rho}) = 2\sum_{nm} \rho_{nm} \int P_{L,nm}(\alpha) \hat{\varrho}(\alpha) d^2\alpha \qquad (7)$$

from which we determine the process superoperator as

$$\mathcal{E}_{lk}^{nm} = 2\int P_{L,nm}(\alpha) \varrho_{lk}(\alpha) d^2\alpha \qquad (8)$$

Before applying the latter result to experiments, a number of practical issues have to be addressed. First, parameter L must be chosen to ensure proper approximation of input states. The second issue is that, in a realistic experiment, the measurement can be done only for coherent
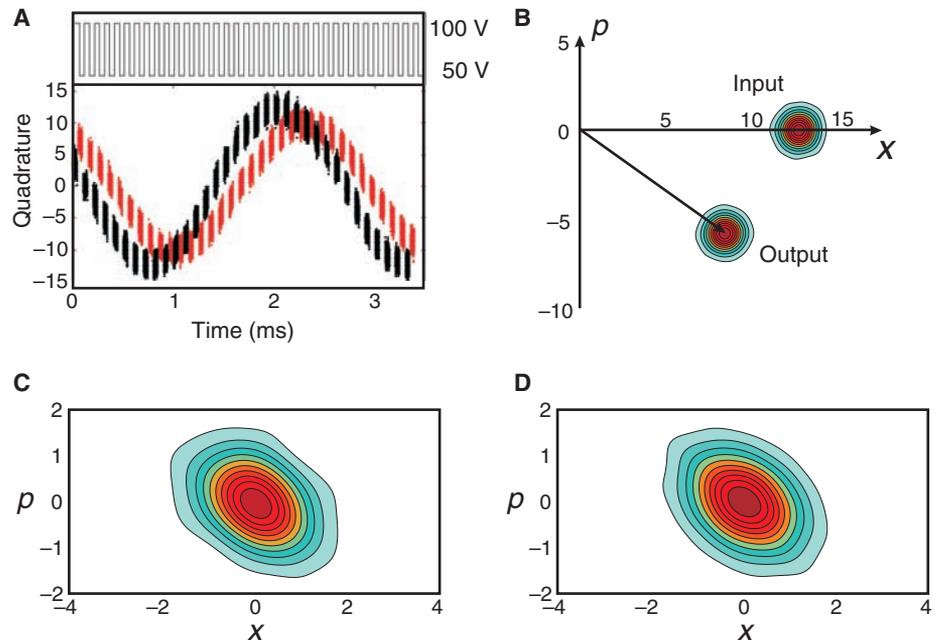
states whose amplitude does not exceed a certain maximum α_{max}. Lastly, the experiment can only be performed with a finite, discrete set of coherent states. Density matrix elements $\varrho_{lk}(\alpha)$ for an arbitrary α, required for calculating the superoperator, must then be obtained by polynomial interpolation. These matters are discussed in (20).

A simplification arises for phase-symmetric processes, in which there is no phase coherence

between the "processing unit" and input states. In this case, if two inputs $\hat{\rho}$ and $\hat{\rho}_1$ are different by an optical phase shift $\hat{U}(\varphi)$, the states $\mathcal{E}(\hat{\rho})$ and $\mathcal{E}(\hat{\rho}_1)$ will differ by the same phase shift:

$$\mathcal{E}[\hat{U}(\varphi)\hat{\rho}\hat{U}^\dagger(\varphi)] = \hat{U}(\varphi)\mathcal{E}(\hat{\rho})\hat{U}^\dagger(\varphi) \qquad (9)$$

Then, if we know the effect of the process on a coherent state $|\alpha\rangle$, we also know what happens to $|\alpha e^{i\varphi}\rangle$, so it is enough to perform measure-
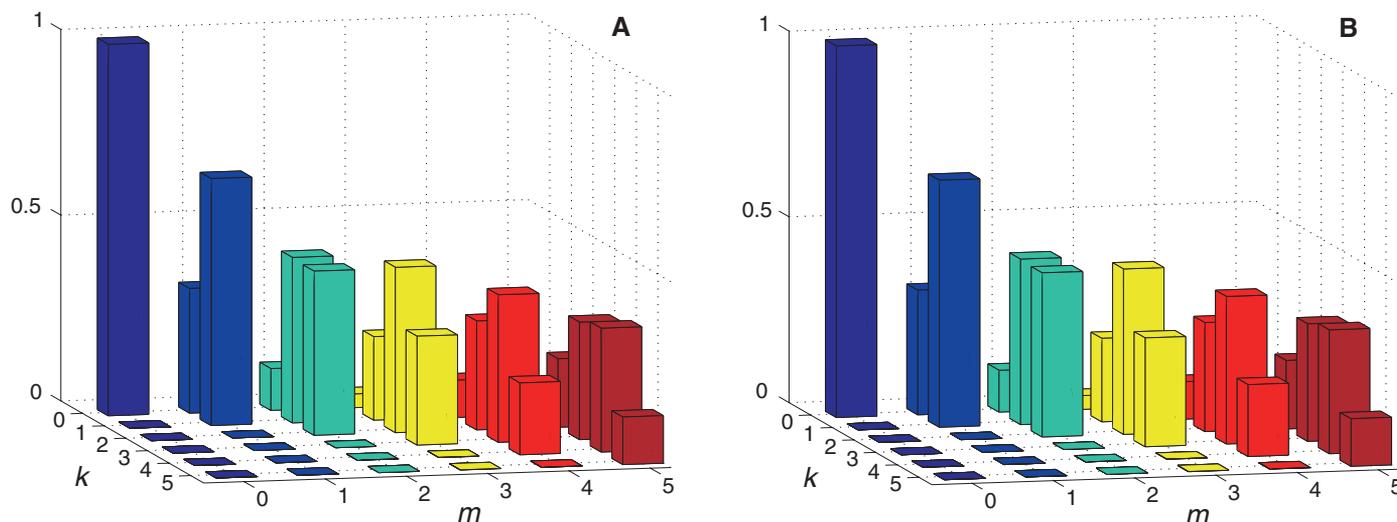

Fig. 2. (**A**) Time-dependent quadrature values acquired from homodyne detection of a coherent state with input $\alpha = 8.3$. Black dots correspond to the state before the process; red dots, after the process. The top curve shows the EOM driving voltage. (**B**) The Wigner function of the coherent state before and after the process. (**C** and **D**) Wigner representations of the measured output squeezed state compared to the one obtained from process tomography.

Fig. 3. The "diagonal" values of the superoperator $\mathcal{E}_{kk}^{mm}$. (**A**) As obtained in the experiment. (**B**) Theoretical model.

ments on input coherent states with real, positive amplitudes. For the process superoperator in the Fock basis, the phase symmetry implies that $\mathcal{E}_{mn}^{kl}$ vanishes unless $k - l = m - n$.

The process studied in our experiment was electrooptical amplitude and phase modulation of the optical field. The process was implemented by using an electrooptical modulator (EOM) followed by a polarizer. The field experienced minimal distortion when a bias voltage $V_1 = 100$ V was applied to the EOM. Switching the voltage to $V_2 = 50$ V produced birefringence and thus losses at the polarizer, along with a phase shift.

A continuous-wave Ti:Sapphire laser at 795 nm was the coherent state source used for the device characterization. We reconstructed the input and output states at 11 different input amplitude levels between $\alpha_1 = 0$ and $\alpha_{11} = 10.9$. In order to keep track of the relative phase shift, we switched the EOM voltage between V_1 and V_2 every 100 μs (Fig. 2A, top), whereas the phase of the local oscillator was linearly scanned by a piezoelectric transducer at 100 Hz. The homodyne photocurrent was recorded with an oscilloscope. To obtain quadrature measurements, we integrated the photocurrent over time intervals of 20 ns. The bottom plot in Fig. 2A shows the recovered quadrature values after normalization to the vacuum noise. The time dependence of the local oscillator phase was recovered from the slow, sinusoidal variation of the average homodyne photocurrent as a function of time.

In this manner, for each input amplitude, we sampled 50,000 phase and quadrature values for both the input and output states and used them to calculate density matrices by likelihood maximization (*15*, *21*) (Fig. 2B). The output state reconstruction showed a phase shift of 36° and a loss of 34% with respect to the input state.

The interpolated experimental data have been used to determine the process superoperator tensor. We used the phase symmetry assumption

in Eq. 9, which is justified by the fact that the EOM driver is independent from the master laser. The elements $\mathcal{E}_{kk}^{mm}$ of the tensor in the photon number basis are plotted in Fig. 3A. This plot should be interpreted as follows: For a given input Fock state $|m\rangle$, the values of $\mathcal{E}_{kk}^{mm}$ give the diagonal elements of the output density matrix. For example, the single-photon state $|1\rangle$ after passing through the EOM will be transformed into a statistical mixture of the single-photon and vacuum states. A theoretical prediction for the process tensor has been calculated by using the Bernoulli transformation to account for a lossy channel and a phase shift superoperator; the superoperator diagonal elements in the Fock basis are displayed in Fig. 3B, and these diagonal elements bear close resemblance to the experimental result. A similar agreement was also obtained for nondiagonal terms of the superoperator, but it is not shown here.

For additional verification, we applied this result to predict the effect of the device on the squeezed vacuum state described in the previous section. This state was produced by pumping an optical parametric amplifier (OPA) in bow-tie configuration with the second harmonic of the Ti:Sapphire laser and using a periodically poled KTiOPO$_4$ crystal as nonlinear medium (*22*, *23*).

The state before (Fig. 1C) and after (Fig. 2C) the process was reconstructed by using homodyne tomography as described above. By applying the process superoperator to the input squeezed state, we predict the process output (Fig. 2D). The maximum quadrature noise variance amounted to 2.19 dB for the measured state and 2.15 dB for the prediction, and the minimum quadrature noise variance was −1.07 dB for the measured state and −0.95 dB for the prediction, corresponding to a quantum fidelity of 0.9935 ± 0.0002.

Whereas here we demonstrate our tomographic method for single-mode inputs, multimode or multichannel processes can be characterized by using multimode P representation, multiple homo-

dyne detectors, and feeding product coherent states as inputs. Our method overcomes substantial limitations of previous optical QPT schemes. Process characterization is not restricted to a Hilbert space associated with a specific qubit and thus reveals the imperfections of a quantum information processing unit. Additionally, it uses only coherent states as inputs, which are readily available from the laser and whose intensities and phases are easily manipulated. This permits characterization of complex processes used in quantum information processing and communication.

References and Notes
1. E. Knill, R. Laflamme, G. J. Milburn, *Nature* **409**, 46 (2000).
2. J. Ye, H. J. Kimble, H. Katori, *Science* **320**, 1734 (2008).
3. N. Gisin, G. Ribordy, W. Tittel, H. Zbinden, *Rev. Mod. Phys.* **74**, 145 (2002).
4. J. F. Poyatos, J. I. Cirac, P. Zoller, *Phys. Rev. Lett.* **78**, 390 (1997).
5. M. A. Nielsen, E. Knill, R. Laflamme, *Nature* **396**, 52 (1998).
6. S. H. Myrskog, J. K. Fox, M. W. Mitchell, A. M. Steinberg, *Phys. Rev. A* **72**, 013615 (2005).
7. J. L. O'Brien *et al.*, *Phys. Rev. Lett.* **93**, 080502 (2004).
8. A. I. Childs, I. L. Chuang, D. W. Lueng, *Phys. Rev. A* **64**, 012314 (2001).
9. M. W. Mitchell, C. W. Ellenor, S. Schneider, A. M. Steinberg, *Phys. Rev. Lett.* **91**, 120402 (2003).
10. G. M. D'Ariano, P. Lo Presti, *Phys. Rev. Lett.* **86**, 4195 (2001).
11. M. Riebe *et al.*, *Phys. Rev. Lett.* **97**, 220407 (2006).
12. J. B. Altepeter *et al.*, *Phys. Rev. Lett.* **90**, 193601 (2003).
13. F. De Martini, A. Mazzei, M. Ricci, G. M. D'Ariano, *Phys. Rev. A* **67**, 062307 (2003).
14. M. Mohseni, A. T. Rezakhani, D. A. Lidar, *Phys. Rev. A* **77**, 032322 (2008).
15. A. I. Lvovsky, *J. Opt. B* **6**, S556 (2004).
16. R. J. Glauber, *Phys. Rev. Lett.* **10**, 84 (1963).
17. E. C. G. Sudarshan, *Phys. Rev. Lett.* **10**, 277 (1963).
18. U. Leonhardt, *Measuring the Quantum State of Light* (Cambridge Univ. Press, Cambridge, 1997).
19. J. R. Klauder, *Phys. Rev. Lett.* **16**, 534 (1966).
20. Materials and methods are available as supporting material on *Science* Online.

21. J. Reháček, Z. Hradil, E. Knill, A. I. Lvovsky, *Phys. Rev. A* **75**, 042108 (2007).
22. J. Appel, D. Hoffman, E. Figueroa, A. I. Lvovsky, *Phys. Rev. A* **75**, 035802 (2007).
23. J. Appel, E. Figueroa, D. Korystov, M. Lobino, A. I. Lvovsky, *Phys. Rev. Lett.* **100**, 093602 (2008).
24. This work was supported by Natural Sciences and Engineering Research Council, Canadian Institute for Advanced Research (CIFAR), Informatics Circle of Research Excellence (iCORE), Alberta Ingenuity Fund, Canada Foundation for Innovation, and QuantumWorks. A.I.L. is a CIFAR scholar, and B.C.S. is a CIFAR associate.

Detection of First-Order Liquid/Liquid Phase Transitions in Yttrium Oxide–Aluminum Oxide Melts

G. N. Greaves,[1]* M. C. Wilding,[1] S. Fearn,[1] D. Langstaff,[1] F. Kargl,[1] S. Cox,[1] Q. Vu Van,[1] O. Majérus,[2] C. J. Benmore,[3] R. Weber,[4] C. M. Martin,[5] L. Hennet[6]

We combine small-angle x-ray scattering (SAXS) and wide-angle x-ray scattering (WAXS) with aerodynamic levitation techniques to study in situ phase transitions in the liquid state under contactless conditions. At very high temperatures, yttria-alumina melts show a first-order transition, previously inferred from phase separation in quenched glasses. We show how the transition coincides with a narrow and reversible maximum in SAXS indicative of liquid unmixing on the nanoscale, combined with an abrupt realignment in WAXS features related to reversible shifts in polyhedral packing on the atomic scale. We also observed a rotary action in the suspended supercooled drop driven by repetitive transitions (a polyamorphic rotor) from which the reversible changes in molar volume (1.2 ± 0.2 cubic centimeters) and entropy (19 ± 4 joules mole^{-1} kelvin^{-1}) can be estimated.

Liquids represent some of the most familiar everyday materials. Recognized by their ability to flow, liquids adopt whatever shape contains them and in suspension form spherical drops. They are the intermediate state between solids and gases, and they extend over temperature and pressure up to sharp phase boundaries along which they coexist with the adjacent states. Phase transitions across these boundaries are discontinuous and of first-order, involving reversible changes in extensive thermodynamic parameters, such as molar volume ΔV and entropy ΔS. Together these parameters define the slope of the phase boundary $dT/dP = \Delta V/\Delta S$ (for instance, the melting curve that separates the liquid from the crystalline state). Phase boundaries themselves can terminate at critical points if the coexistent phases become indistinguishable, the most well-known being the formation of fluids from their liquid and vapor states.

The physics of phase transitions and critical phenomena is extensive (*1*). It also includes the wealth of crystalline phases within the solid state where periodic structures can abruptly transform under pressure and temperature into new crystal-line states distinct in density and symmetry (*2*). One of the most exciting developments in liquid state science is the growing evidence for different phases of the same liquid and for phase transitions between them at characteristic temperatures and pressures (*3–7*). At first glance such "polyamorphism" is counterintuitive, as diffusion processes in a liquid would appear to lead to the same time-averaged

aperiodic structure. However, unlike crystals, liquids are characterized by temporal and spatial fluctuations in density (*1*). These potentially could be the antecedents for different self-assembled phases distinguished by density and entropy (*7*), particularly in the metastable supercooled state where liquid flow becomes increasingly viscous with falling temperature or increasing pressure. As the concept of polyamorphism has developed, the so called "two-state model" (*8, 9*) has proved influential in defining the phase boundary between a low-density liquid (LDL) phase and a high-density liquid (HDL) phase straddled by spinodal limits. This is illustrated in Fig. 1. In particular, there is a critical point *C* on the phase boundary below which the LDL and HDL states coexist and beyond which the liquid is single phase. If *C* lies at negative pressures, a liquid/liquid phase transition between HDL and LDL states is expected at ambient pressure and characteristic temperature T_{LL} (Fig. 1).

Speculation about the existence of liquid polyamorphs has its origins in the effort to better explain negative melting curves [i.e., $dT/dP < 0$ (*3, 5, 7–9*)] for which the fusion of ice is the most familiar (*10*). Even though transitions between polyamorphic states in water have now been well-studied (*3, 11–15*), controversy still exists as to whether these are truly of first-order character (*13, 14*), analogous to phase transitions in the crystalline solid state (*2*), or whether they occur via numerous intermediate glassy states (*12, 15*).

[1]Centre for Advanced Functional Materials and Devices, Institute of Mathematics and Physics, Aberystwyth University, Aberystwyth SY23 3BZ, UK. [2]Ecole Nationale Supérieure de Chimie de Paris, 11 rue Pierre et Marie Curie, 75231, Paris, France. [3]Advanced Photon Source, Argonne National Laboratory, Argonne, IL 60439, USA. [4]Materials Development, 3090 Daniels Court, Arlington Heights, IL 60004, USA. [5]Synchrotron Radiation Source, STFC Daresbury Laboratory, Warrington, Cheshire, WA4 4AD, UK. [6]CNRS-CEMHTI, 1d Avenue de la Recherche Scientifique, 45071 Orléans Cedex 9, France.

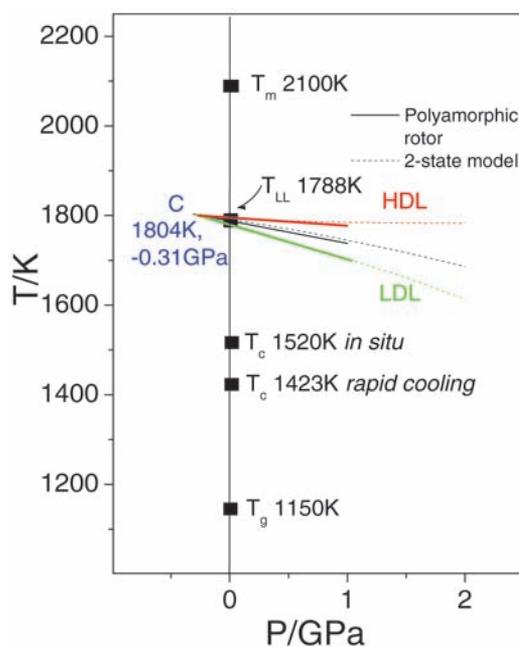*To whom correspondence should be addressed. E-mail: gng@aber.ac.uk

Fig. 1. *T/P* phase boundary separating HDL and LDL phases surrounded by spinodal limits. Dashed curves represent calculations from the two-state model (*8, 9*). Solid curves indicate $dT/dP = \Delta V_{LL}/\Delta S_{LL}$, as determined from the changes in entropy ΔS_{LL} and molar volume ΔV_{LL} for supercooled AY20, with ±σ limits taken from Fig. 3C. This places the critical point *C* at 1804 K and −0.31 GPa. T_m and the HDA T_g for AY20 are also included (*26, 31*), together with T_c taken from Fig. 3B and from rapid quenching (*29*).